THE JOURNAL OF BIOLOGICAL CHEMISTRY VOL. 287, NO. 36, pp. 30385–30394, August 31, 2012

Nucleotide Binding Site Communication in *Arabidopsis thaliana* Adenosine 5′-Phosphosulfate Kinase*

Received for publication, May 30, 2012, and in revised form, July 3, 2012 Published, JBC Papers in Press, July 18, 2012, DOI 10.1074/jbc.M112.387001

Geoffrey E. Ravilious and Joseph M. Jez[1]

From the Department of Biology, Washington University, St. Louis, Missouri 63130

Background: Adenosine 5′-phosphosulfate kinase (APSK) catalyzes the synthesis of phosphoadenosine 5′-phosphosulfate, but how APSK coordinates binding of phosphonucleotides is unclear.
Results: Using calorimetry, crystallography, and mutagenesis, this study provides new insight on nucleotide binding in APSK.
Conclusion: The P-loop and a critical aspartate integrate dynamic structural and nucleotide recognition features.
Significance: These results suggest how structural changes guide the order of nucleotide addition for catalysis.

Adenosine 5′-phosphosulfate kinase (APSK) catalyzes the ATP-dependent synthesis of adenosine 3′-phosphate 5′-phosphosulfate (PAPS), which is an essential metabolite for sulfur assimilation in prokaryotes and eukaryotes. Using APSK from *Arabidopsis thaliana*, we examine the energetics of nucleotide binary and ternary complex formation and probe active site features that coordinate the order of ligand addition. Calorimetric analysis shows that binding can occur first at either nucleotide site, but that initial interaction at the ATP/ADP site was favored and enhanced affinity for APS in the second site by 50-fold. The thermodynamics of the two possible binding models (*i.e.* ATP first *versus* APS first) differs and implies that active site structural changes guide the order of nucleotide addition. The ligand binding analysis also supports an earlier suggestion of intermolecular interactions in the dimeric APSK structure. Crystallographic, site-directed mutagenesis, and energetic analyses of oxyanion recognition by the P-loop in the ATP/ADP binding site and the role of Asp^{136}, which bridges the ATP/ADP and APS/PAPS binding sites, suggest how the ordered nucleotide binding sequence and structural changes are dynamically coordinated for catalysis.

All organisms acquire and assimilate sulfate and/or sulfide for the synthesis of a wide array of metabolites (1–5). Chemical activation of sulfate in organisms that assimilate sulfur from the environment is carried out by ATP sulfurylase and yields adenosine 5′-phosphosulfate (APS)[2] (5). In prokaryotes, fungi, and mammals, APS kinase (APSK; also known as adenylyl-sulfate kinase; EC 2.7.1.25) catalyzes the ATP-dependent phosphorylation of APS into PAPS, which is used for sulfur assimilation and as a biosynthetic sulfate donor (1–5). In plants, the sulfur assimilatory pathway branches after formation of APS into primary and secondary pathways. The reductive (*i.e.* primary) route leads to the production of sulfur-containing amino acids and peptides (2–6). The second metabolic route begins with APS kinase and synthesizes PAPS as a sulfate donor for the sulfonation of brassinosteroids, peptide hormones, and molecules critical for protection against herbivores, such as glucosinolates (8–10). Glucosinolate synthesis also requires metabolites produced by the primary sulfur assimilatory pathway (11–14). PAPS is also a precursor of 3′-phosphoadenosine 5′-phosphate, which is a critical metabolite for stress gene regulation and plant development (15). Control of sulfate flux between the primary (reductive) and secondary metabolic routes in plants helps to maintain the synthesis of the metabolites essential for plant growth and responses to different stresses (11–19).

In *Arabidopsis thaliana*, APSK is necessary for plant growth and directly connects the sulfur assimilation pathway to the biosynthesis of sulfonated molecules (11–14), but the biochemical regulation of this critical branch point enzyme in plant metabolism is largely unexamined. Initial studies of APSK from *A. thaliana* (AtAPSK) revealed severe substrate inhibition by APS, as observed in the enzyme from fungi, bacteria, and mammals (7, 20–23); this inhibition presumably results from formation of an *E*·ADP·APS dead-end complex (22, 24). Steady-state kinetic studies of the *Penicillium chrysogenum* APSK are consistent with a sequential ordered reaction mechanism in which ATP binds first, followed by APS (20), although later studies of the *Escherichia coli* APSK suggested that the order of ATP *versus* APS addition is random and varies with ligand concentrations (21) (Fig. 1*A*).

Crystal structures of APSK from *Arabidopsis* (Fig. 1*B*) and *P. chrysogenum,* the APSK domain from human PAPS synthetase, and the bifunctional ATP sulfurylase-APSK from *Aquifex aeolicus* and *Thiobacillus denitrificans* (25–30) show that the overall fold of APSK is highly conserved across a variety of organisms. Two nucleotide-binding sites (*i.e.* ATP/ADP and APS/PAPS sites) span the core α/β-purine nucleotide-binding domain and are capped by a smaller α-helical "lid" domain, which is disordered in the absence of ligands (26). The interface between the

* This work was supported by National Science Foundation Grant MCB-0904215.

The atomic coordinates and structure factors (code 4FXP) have been deposited in the Protein Data Bank, Research Collaboratory for Structural Bioinformatics, Rutgers University, New Brunswick, NJ (http://www.rcsb.org/).

[1] To whom correspondence should be addressed: One Brookings Dr., Campus Box 1137, St. Louis, MO 63130. Tel.: 314-935-3376; E-mail: jjez@biology2.wustl.edu.

[2] The abbreviations used are: APS, adenosine 5′-phosphosulfate; AMP-PNP, β,γ-imidoadenosine-5-triphosphate; APSK, adenosine-5′-phosphosulfate kinase, also known as adenylyl-sulfate kinase; AtAPSK, *Arabidopsis thaliana* APSK; ATPγS, adenosine 5′-(γ-thio)triphosphate; βME, β-mercaptoethanol; ITC, isothermal titration calorimetry; PAPS, adenosine 3′-phosphate 5′-phosphosulfate.

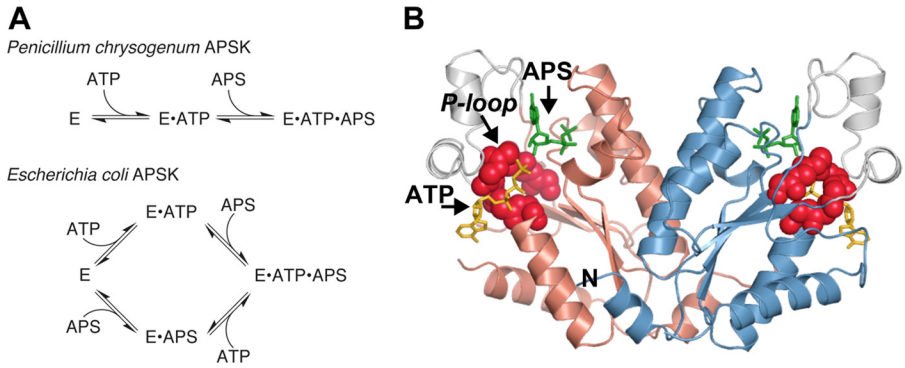

FIGURE 1. **Overview of APSK nucleotide binding and structure.** *A,* schematic of ordered and random nucleotide binding proposed for APSK from *P. chrysogenum* and *E. coli*, respectively. *B,* structural overview of AtAPSK and nucleotide binding sites. The ribbon diagram of AtAPSK (24) shows the core α/β-nucleotide binding domain (*rose* and *blue* in each monomer of the dimer) and the smaller active site capping domain (*gray*). APS (*green*) and ATP (*yellow*) bound in their respective nucleotide binding sites are shown in each active site of the dimer. Residues of the P-loop are shown as a space-filling model (*red*). The position of the N-terminal α-helix is indicated by the letter *N*.

ATP/ADP and APS/PAPS binding sites is spanned by a canonical P-loop or Walker A motif (Ser^{110}-Thr^{116} in AtAPSK), as observed in the structures of all nucleotide kinases (31, 32). Kinetic studies of the *P. chrysogenum* APSK suggest that APS binds tighter in the presence of ADP and magnesium compared with the unliganded enzyme, which has also been proposed as the basis for substrate inhibition (22); however, these studies relied on enzymatic assays to infer details about the nucleotide binding mechanism. Overall, steady-state kinetic studies and multiple crystal structures of APSK from a variety of species imply that dynamic features around the active site contribute to nucleotide binding.

Using a combination of isothermal titration calorimetry (ITC), x-ray crystallography, and kinetic analysis of point mutants, we examine the formation of AtAPSK nucleotide complexes and probe the role of active site features that coordinate the order of ligand addition. Although energetic analysis of complex formation showed that nucleotides can bind to either the ATP/ADP or APS/PAPS site, initial binding at the ATP/ADP site was favored and enhanced affinity for APS. Interestingly, the thermodynamics of each of the possible binding orders differs, likely reflecting different structural changes associated with nucleotide binding at each site to communicate binding site occupancy. Crystallographic and energetic analysis of oxyanion recognition by the P-loop and a critical aspartate residue that bridges the two nucleotide binding sites of AtAPSK provides insight on how an ordered sequence of binding events and structural changes are coordinated for efficient catalysis.

EXPERIMENTAL PROCEDURES

Reagents—All chemicals and reagents were of analytical grade and purchased from Sigma. The standard experimental buffer condition was 25 mM HEPES, pH 7.5, 200 mM KCl, 5% (v/v) glycerol, and either 1 mM Tris(2-carboxyethyl)phosphine or 5 mM β-mercaptoethanol (βME), unless stated otherwise. Either reducing agent prevented formation of intermonomer disulfide bonds (25), as judged by nonreducing SDS-PAGE of samples taken before and after ITC titrations.

Protein Expression, Purification, and Site-directed Mutagenesis—The pET-28a-AtAPSKΔ77 bacterial expression construct, which encodes *A. thaliana* APSK isoform 1 lacking the plastid localization sequence (residues 1–77) and with an N-terminal His_6 tag, was previously described (33). Protein overexpression in *E. coli* BL21(DE3) and purification by nickel affinity and gel-filtration chromatographies were described previously (25), with some modifications. For cell lysis and nickel affinity chromatography, all buffers were supplemented with 5 mM βME. After affinity purification, the protein was dialyzed into 25 mM HEPES, pH 7.5, 200 mM KCl, 5% glycerol, and 5 mM dithiothreitol (DTT), then loaded onto a Superdex-200 26/60 HiLoad FPLC size exclusion column equilibrated in the same buffer. Calibration of the size exclusion column was performed as described previously (34). Purified protein was either flash frozen in liquid nitrogen and stored at −80 °C or dialyzed against 25 mM HEPES, pH 7.5, 200 mM KCl, 5% glycerol, and either 1 mM Tris(2-carboxyethyl)phosphine or 5 mM βME for use in ITC experiments. Site-directed mutants of AtAPSK (G111A, G113A, D136N, and D136A) were generated using the QuikChange PCR method (Agilent) with expression and purification as above.

Calorimetric Measurements—ITC experiments were performed using a VP-ITC calorimeter (Microcal, Inc.). AtAPSK was dialyzed at 4 °C in 25 mM HEPES, pH 7.5, 200 mM KCl, 5% glycerol, and either 1 mM Tris(2-carboxyethyl)phosphine or 5 mM βME. Stock solutions (100 mM) of ATP, ATPγS, AMP-PNP, ADP, and APS were dissolved in NaOH to attain a pH of 7.5 and stored at −20 °C. Prior to ITC experiments, appropriate dilutions were made with dialysis buffer. Protein and nucleotide solutions were degassed at room temperature prior to use. For each titration, 20 to 30 injections of 10 μl of nucleotide were added into sample solutions containing protein (60–100 μM) in the presence or absence of ligands and/or 5 mM Mg^{2+}. AtAPSK complexed with AMP-PNP, ADP, or APS was formed by incubating protein and 2 mM AMP-PNP, 500 μM ADP, or 2 mM APS overnight (4 °C) followed by a 4-h equilibration at 17 °C before titrations. Data were analyzed using either a one-site (*i.e.* identical sites) binding model (Equation 1) or a two-site binding model (Equation 2), as follows,

$$Q_i^{tot} = V_0 \cdot M_i^{tot} \cdot ((nK_1x)\Delta H_1)/1 + K_1x) \quad \text{(Eq. 1)}$$

$$Q_i^{tot} = V_0 \cdot M_i^{tot} \cdot ((K_1x\Delta H_1 + (\Delta H_1 + \Delta H_2)K_1K_2x^2)/(1 + K_1x + K_1K_2x^2)) \quad \text{(Eq. 2)}$$

TABLE 1
Summary of crystallographic statistics for the AtAPSK·APS·SO_4^{2-} complex

Crystal	
Space group	C2
Cell dimensions	a = 120.9 Å, b = 92.35 Å, c = 73.18 Å; β = 113.5°
Data collection	
Wavelength (Å)	0.979
Resolution range (Å) (highest shell resolution)	33.9–1.95 (2.02–1.95)
Reflections (total/unique)	163,947/46,572
Completeness (highest shell)	95.5% (100.0%)
$\langle I/\sigma \rangle$ (highest shell)	38.5 (5.0)
R_{sym} [a] (highest shell)	5.2% (15.1%)
Model and refinement	
R_{cryst} [b]/R_{free} [c]	16.1/19.0
No. of protein atoms	4,738
No. of water molecules	435
No. of ligand atoms	96
Root mean square deviation, bond lengths (Å)	0.006
Root mean square deviation, bond angles (°)	0.97
Average B-factor (Å^2), protein, waters, ligands	38.7, 46.5, 39.2
Stereochemistry, most favored, allowed, generously allowed	96.7, 3.1, 0.2%

[a] $R_{sym} = \Sigma|I_h - \langle I_h \rangle|/\Sigma I_h$, where $\langle I_h \rangle$ is the average intensity over symmetry.
[b] $R_{cryst} = \Sigma||F_o| - |F_c||/\Sigma|F_o|$, where summation is over the data used for refinement.
[c] R_{free} is defined the same as R_{cryst}, but was calculated using 5% of data excluded from refinement.

where Q_i^{tot} is the total heat after the ith injection, V_0 is the calorimetric cell volume, M_i^{tot} is the concentration of protein in the cell after the ith injection, ΔH is the corresponding enthalpy change to AtAPSK·nucleotide binding, n is the number of nucleotide binding sites on the APSK dimer, and K is the equilibrium binding constant. In the latter, k_1 and k_2 are the observed binding constants for the first and second sites, ΔH_1 and ΔH_2 are the corresponding enthalpy changes upon nucleotide binding to each site, and $p = 1 + k_1X_i + k_1k_2X$. Fitting of data were performed using Origin software.

Enzyme Assays—All steady-state kinetic analysis was performed as previously described using an enzyme-coupled spectrophotometric assay (25).

Crystallography—Crystals of the AtAPSK·APS·SO_4^{2-} complex were formed as follows. Crystals of AtAPSK in complex with APS were first grown at 4 °C in hanging drops with a 1:1 ratio of protein (~10 mg ml^{-1}) and crystallization buffer (100 mM HEPES, pH 7.25, 200 mM $MgCl_2$, and 15–17.5% PEG-2000) supplemented with 5 mM APS. For x-ray data collection, crystals were transferred to a cryoprotectant solution of mother liquor containing 20% glycerol and 10 mM SO_4^{2-}. Crystals were frozen in liquid nitrogen after a 2-h incubation period. X-ray diffraction data were collected at SBC beamline 19-ID of the Advanced Photon Source, Argonne National Laboratory. The HKL3000 software suite was used to integrate, merge, and scale diffraction intensities (35). The structure of the AtAPSK·APS·SO_4^{2-} complex was solved by molecular replacement with PHASER (36) using the previously determined AtAPSK structure (25) with ligands and water molecules removed as a search model. The model was built in COOT (37) and refined using PHENIX (38) until the R-factors converged to those reported in Table 1. Coordinates and structure factors for the AtAPSK·APS·SO_4^{2-} complex have been deposited in the Protein Data Bank (code 4FXP).

RESULTS

Calorimetric Analysis of Nucleotide Binding to AtAPSK—To compare nucleotide binding to AtAPSK, ITC experiments were performed using ATP, the ATP analogues AMP-PNP and ATPγS, ADP, and APS in the presence and absence of Mg^{2+} (Fig. 2, Table 2). All nucleotides showed exothermic binding. Fitting of the ITC data to a one-site binding model failed to adequately describe the observed results, whereas, satisfactory fits were obtained using a two-site binding model with stoichiometries consistent with the binding of two nucleotides per AtAPSK dimer. In all cases, the K_d value of the second site for each nucleotide was 5- to 30-fold higher than the first site, suggesting potential cross-talk between nucleotide binding sites in the homodimer.

Titration of AtAPSK with ATP, AMP-PNP, and ATPγS showed that the ATP binding site is sensitive to changes in the phosphoanhydride chemical structure (Fig. 2*A*, Table 2). Substitution of one of the γ-phosphate oxygens with a sulfur in ATPγS increased affinity 5-fold compared with ATP. In contrast, replacement of the oxygen linking the β- and γ-phosphates with a nitrogen (AMP-PNP) decreased affinity 15-fold. As suggested by steady-state kinetic experiments (22), ADP bound with a 7-fold tighter affinity than ATP (Fig. 2*B*, Table 2). In the presence of Mg^{2+}, AtAPSK hydrolyzed ATP and ATPγS, which prevented accurate binding analysis with these ligands. Addition of Mg^{2+} had little effect on binding of the first AMP-PNP molecule, but modestly improved affinity for the second molecule by 4-fold (Fig. 2*A*, Table 2). An opposite effect was observed with ADP and Mg^{2+}, which decreased ligand affinity 10-fold (Fig. 2*B*, Table 2). To determine whether this change resulted from the ion or increased ionic strength, titrations of AtAPSK with ADP at 0.5 M KCl and NaCl were performed and did not alter the titration profile or the measured parameters, which indicates that the observed decrease in affinity for ADP is a Mg^{2+}-specific effect. Binding of APS was weaker than ATP and was insensitive to Mg^{2+} (Fig. 2*C*, Table 2), which is consistent with the location of the ion in the ATP/ADP, not APS/PAPS, binding site of AtAPSK (25).

Calorimetric Analysis of AtAPSK·Nucleotide Ternary Complex Formation—Analysis of single nucleotide interaction with AtAPSK showed that binding at either the ATP/ADP or APS/PAPS site did not require ordered ligand addition. ITC experiments were used to determine whether pre-formed complexes of AtAPSK and either phosphonucleotide (AMP-PNP and ADP) or APS affected the affinity for binding of APS or phosphonucleotides, respectively. First, we compared binding of APS to pre-formed AMP-PNP and ADP complexes, which is the binding order proposed for APSK from *P. chrysogenum* and the upper path suggested for the *E. coli* enzyme (Fig. 1*A*).

Addition of APS to AtAPSK·AMP-PNP in the presence or absence of Mg^{2+} yielded similar K_d values (Fig. 3*A*, Table 3), which were ~50-fold tighter than APS binding to the unliganded enzyme (Table 2). APS binding to the AtAPSK·ADP complex displayed less than 2-fold differences compared with APS binding to the AtAPSK·AMP-PNP complex; however, the presence of Mg^{2+} altered the binding model with a 5-fold improvement in K_d for the first binding event and a 4-fold decrease in

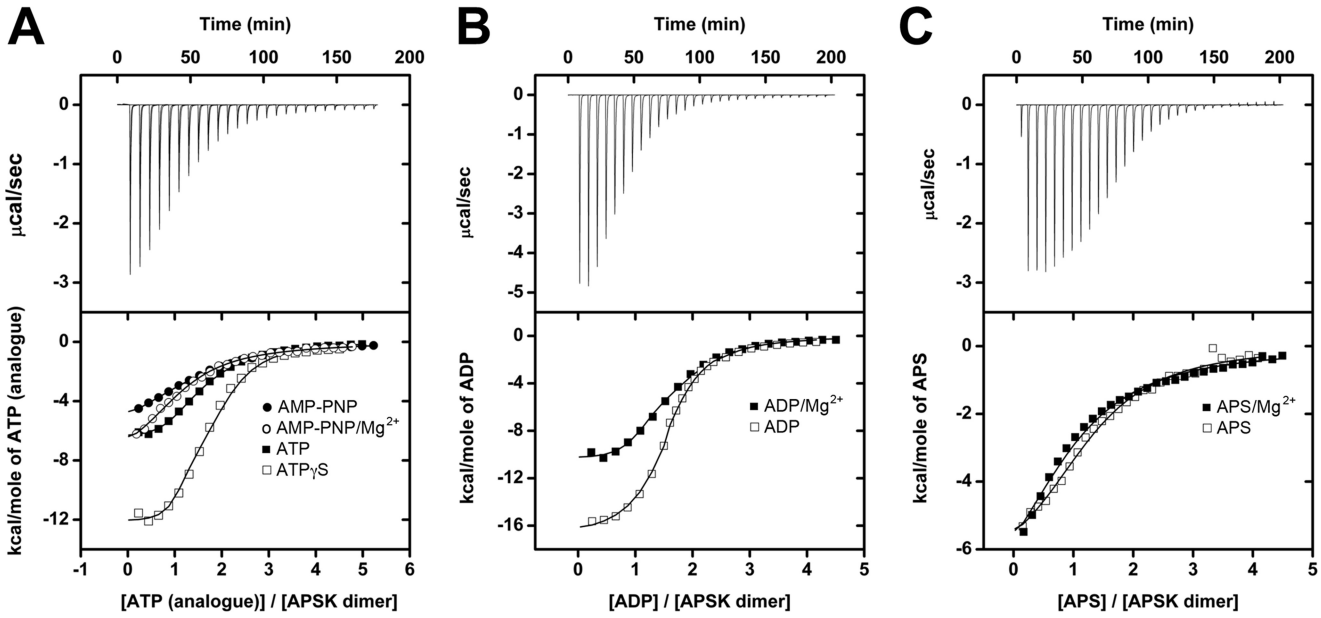

FIGURE 2. **ITC analysis of nucleotide binding to AtAPSK.** *A,* titration of AtAPSK with ATP (*solid squares*), ATPγS (*open squares*), AMP-PNP (*closed circles*), and AMP-PNP + 5 mM Mg^{2+} (*open circles*). *B*, titration of AtAPSK with ADP (*open squares*) and ADP + 5 mM Mg^{2+} (*solid squares*). *C*, titration of AtAPSK with APS (*open squares*) and APS + 5 mM Mg^{2+} (*solid squares*). Representative experimental data for the ATP (*A*), ADP (*B*), and APS (*C*) titrations are plotted as heat signal (µcal s^{-1}) *versus* time (min) in each *upper panel*. Each experiment consisted of 20 to 30 injections of 10 µl each of nucleotide into a solution containing AtAPSK dimer. Each *lower panel* shows the integrated heat responses per injection. The *solid line* is the linear regression fit using a two-site binding model (see Table 2).

TABLE 2

Thermodynamic parameters of nucleotide binding to AtAPSK

All titrations were performed at 17 °C with resulting data fit to a two-site binding model as described under "Experimental Procedures."

Ligand	K_1	K_2	ΔH_1	ΔH_2
	µM		*kcal mol*$^{-1}$	
ATP	1.25 ± 0.09	24.7 ± 6.9	−6.4 ± 0.7	−5.0 ± 0.7
ATPγS	0.26 ± 0.05	7.9 ± 0.1	−12.2 ± 0.4	−5.2 ± 0.3
AMP-PNP	19.6 ± 1.5	361 ± 45	−4.8 ± 0.5	−1.2 ± 0.6
AMP-PNP + 5 mM Mg^{2+}	16.4 ± 0.2	82.6 ± 7.7	−6.0 ± 0.1	−3.3 ± 0.4
ADP	0.18 ± 0.05	4.8 ± 0.6	−16.5 ± 0.2	−9.4 ± 0.1
ADP + 5 mM Mg^{2+}	1.8 ± 0.4	38.1 ± 4.2	−10.7 ± 0.8	−6.2 ± 1.6
APS	66.7 ± 10.5	325 ± 89	−5.6 ± 0.9	−1.9 ± 0.7
APS + 5 mM Mg^{2+}	80.4 ± 5.2	460 ± 99	−5.1 ± 2.3	−2.2 ± 0.8

affinity for binding of at the second site (Fig. 3*B,* Table 3). These results agree with previous kinetic experiments using the fungal APSK, which found that Mg^{2+} was required for ADP to increase the affinity for APS (22). In the absence of Mg^{2+}, APS binding to either the AMP-PNP or ADP complex was best fit to a one-site binding model, whereas, a two-site model best described binding of APS in the presence of Mg^{2+}. These results provide strong evidence for unidirectional synergistic binding, which would explain the obligate binding order of ATP followed by APS suggested by earlier steady-state kinetic studies of APSK (24).

In the other possible binding sequence (*i.e.* APS first; Fig. 1*A*), the effect of forming the AtAPSK·APS complex on either AMP-PNP or ADP binding was less than 6-fold different compared with the unliganded enzyme titration (Fig. 3*C,* Table 3). Analysis of the interaction between the AtAPSK·APS complex and AMP-PNP required a two-site binding model. In contrast, the isotherm resulting from ADP titration could be described by a one-site binding model with a 2:1 stoichiometry of ligand to dimer, suggesting that APS does not bind with significant affinity to the ATP/ADP binding site. The affinity of AtAPSK for AMP-PNP improved an order of magnitude in the presence of APS, whereas the affinity for ADP was not significantly changed. The increased affinity for AMP-PNP, but not ADP, may result from interactions formed between the γ-phosphate of AMP-PNP and active site residues.

Surprisingly, binding of AMP-PNP to the AtAPSK·APS complex showed an endothermic interaction (Fig. 3*C,* Table 3), which markedly contrasts with the exothermic binding displayed by nucleotides to either unliganded or liganded enzyme. Although binding of nucleotides to AtAPSK can occur in either order (Fig. 1*A*), the two possible routes leading to formation of the AtAPSK·ATP·APS ternary complex are not thermodynamically equal. This difference in binding energetics may reflect structural and/or dynamic differences in the active site that correspond to the order of ligand addition.

Calorimetric, Crystallographic, and Mutagenesis Analysis of P-loop Recognition of Oxyanions—The above results, along with crystal structures of APSK from a variety of sources (25–30), suggests that the P-loop (Fig. 1*B*) plays a role in nucleotide binding specificity at the ATP/ADP site of AtAPSK. We tested the ability of the P-loop to discern ligands based on anhydride size and charge density by using a series of oxyanions: SO_4^{2-}, PO_4^{2-}, NO_3^-, CO_3^-, and ClO_3^-. Titrations of AtAPSK with SO_4^{2-}

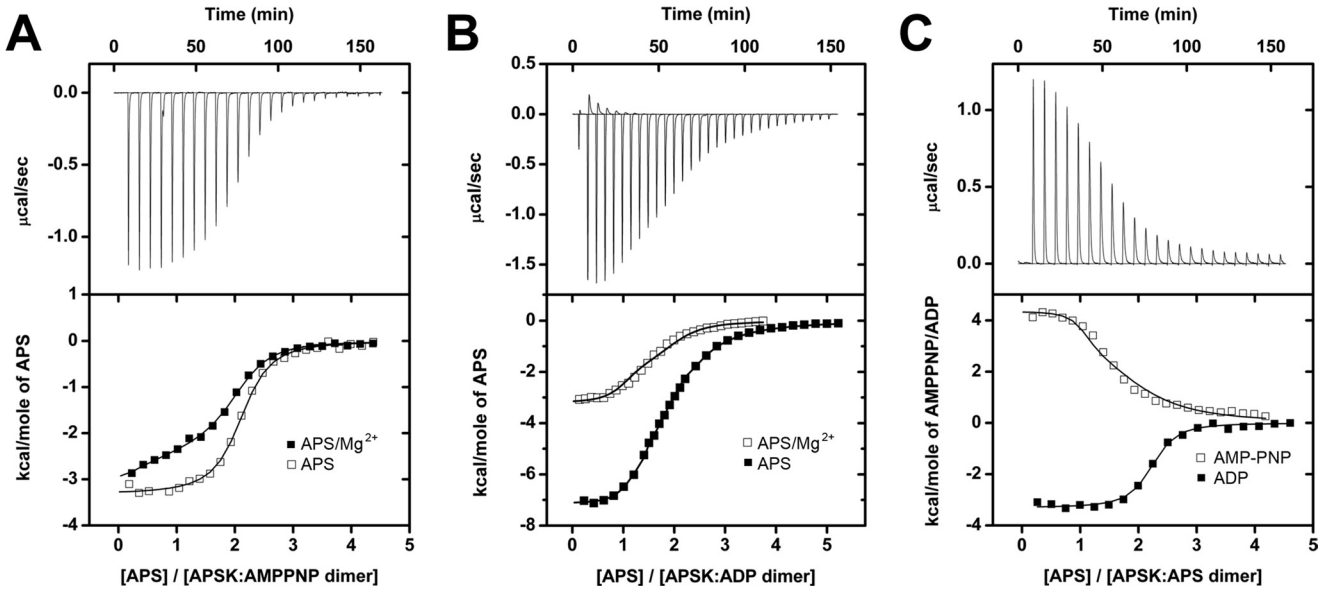

FIGURE 3. **ITC analysis of nucleotide binding to AtAPSK·nucleotide complexes.** *A,* titration of AtAPSK·AMP-PNP with APS (*open squares*) and APS + 5 mM Mg^{2+} (*solid squares*). *B,* titration of AtAPSK·ADP with APS (*solid squares*) and APS + 5 mM Mg^{2+} (*open squares*). *C,* titration of AtAPSK·APS with AMP-PNP (*open squares*) and ADP (*solid squares*). Representative experimental data for the APS (*A* and *B*) and AMP-PNP (*C*) titrations are plotted as heat signal (μcal s^{-1}) *versus* time (min) in each *upper panel*. Each experiment consisted of 20 to 30 injections of 10 μl each of nucleotide into a solution containing AtAPSK dimer and either 0 or 5 mM Mg^{2+}. Each *lower panel* shows the integrated heat responses per injection. The *solid line* is the linear regression fit using either a one- or two-site binding model (see Table 3).

TABLE 3

Thermodynamic parameters of nucleotide binding to AtAPSK·nucleotide complexes

All titrations were performed at 17 °C as described under "Experimental Procedures." AtAPSK·nucleotide complexes were pre-formed either in the absence or presence of 5 mM Mg^{2+}. ITC data were fit to either a one-site binding model (n = number of sites) or a two-site binding model.

Pre-bound nucleotide	Titrant	K_1	K_2	ΔH_1	ΔH_2
		μM		*kcal mol*$^{-1}$	
AMP-PNP	APS	1.50 ± 0.10 n = 2.00 ± 0.10		−3.3 ± 0.1	
AMP-PNP·Mg^{2+}	APS	1.50 ± 0.60	3.60 ± 0.40	−4.4 ± 0.1	−2.3 ± 0.1
ADP	APS	3.30 ± 0.70 n = 1.93 ± 0.05		−7.2 ± 0.1	
ADP·Mg^{2+}	APS	0.60 ± 0.20	12.9 ± 3.8	−3.1 ± 0.4	−2.4 ± 0.5
APS	AMP-PNP	3.10 ± 0.40	18.6 ± 0.9	4.3 ± 0.6	3.0 ± 0.2
APS	ADP	0.65 ± 0.04 n = 2.00 ± 0.10		−3.3 ± 0.4	

resulted in an exothermic heat change (Fig. 4*A*), but weak binding did not allow for accurate curve fitting. No heat change was observed in titrations with other oxyanions (Fig. 4*A*). To probe the location of SO_4^{2-} binding, AtAPSK preincubated with 10 mM SO_4^{2-} was titrated with ATP, ADP, and APS. Preincubation abrogated binding of ATPγS and ADP (Fig. 4*B*). In contrast, pre-formation of the AtAPSK·SO_4^{2-} complex resulted in 10- to 100-fold improvement in binding affinity for APS (Fig. 4*C,* Table 4), analogous to the effect observed with formation of the AtAPSK·AMP-PNP and AtAPSK·ADP complexes. These results suggest that the sulfate-binding site is likely located within the ATP/ADP site, which was confirmed by x-ray crystallography.

The 1.95-Å resolution x-ray crystal structure of the AtAPSK·APS·SO_4^{2-} complex was solved by molecular replacement (Table 1, Fig. 5). The overall structure is similar to that of the AtAPSK·AMP-PNP·APS complex (25) with the root mean square deviation of Cα-atoms at 0.37 $Å^2$. Clear electron density for bound APS was observed in the active site with additional discontinuous density near the P-loop of the ATP/ADP binding site (Fig. 5*A*), which was modeled as SO_4^{2-}. Multiple interactions were formed between the SO_4^{2-} and residues in the P-loop (Fig. 5*B*), including main chain contacts from Gly^{111}, Ser^{112}, Gly^{113}, Lys^{114}, and Ser^{115} and hydrogen bonds from the hydroxyl group of Ser^{115} and amine of Lys^{114} (Fig. 5*B*). Compared with the AtAPSK·AMP-PNP·APS complex (Fig. 5, *C* and *D*), the position of the SO_4^{2-} corresponds to that of the β-phosphate of AMP-PNP with a nearly identical set of interactions formed in each structure.

To further examine the role of the P-loop in AtAPSK, two site-directed mutants (G111A and G113A) were generated to disrupt the ATP/ADP binding site. Each mutant protein was catalytically inactive. ITC analysis of ATPγS binding to the G111A mutant showed a negligible enthalpy change, although the binding affinity for APS was comparable with binding to the unliganded wild-type enzyme (Fig. 4*D,* Table 4). Similar results were observed for the G113A mutant (Table 4). Each mutant also disrupted SO_4^{2-} binding, as there was no heat signature detected by ITC. These results underscore the importance of the P-loop for ATP/ADP binding.

Asp^{136} as a Critical Determinant of APS Substrate Inhibition and Nucleotide Binding Order—The increased affinity of the plant and fungal APSK (22) for APS, when in complex with ADP, support a model in which APS-dependent substrate inhibition results from formation of a dead-end complex. We examined the structure of AtAPSK (25) to identify residues

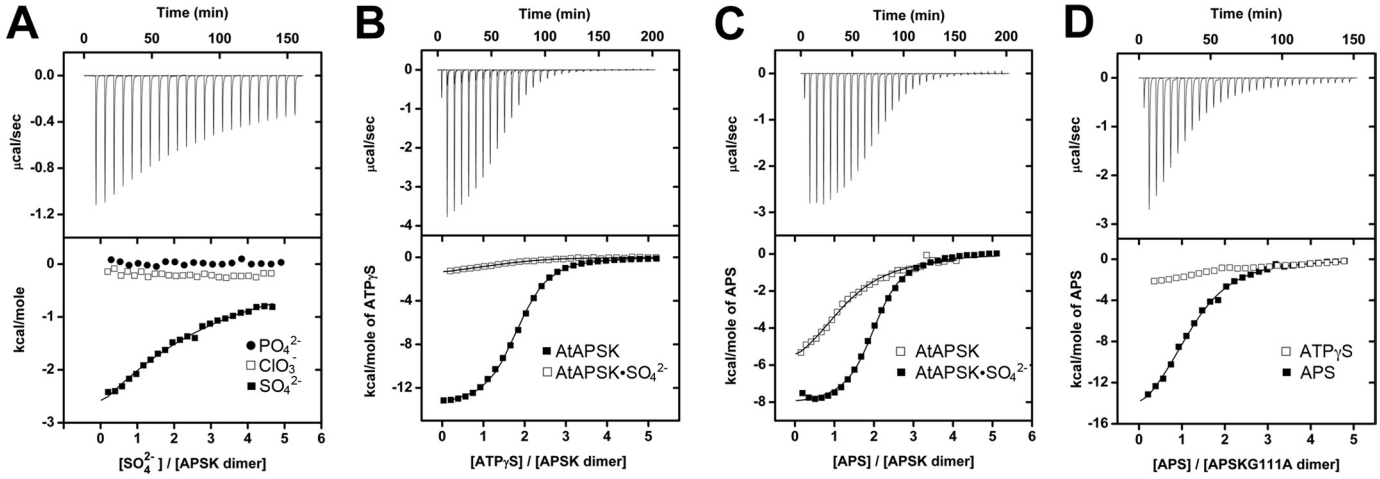

FIGURE 4. **ITC analysis of oxyanion binding to AtAPSK and nucleotide binding to the AtAPSK·SO_4^{2-} complex.** *A*, titration of AtAPSK with SO_4^{2-} (*closed squares*), ClO_3^- (*open squares*), and PO_4^{2-} (*closed circles*). *B*, titration of AtAPSK (*closed squares*) and AtAPSK·SO_4^{2-} (*open squares*) with ATPγS. *C*, titration of AtAPSK (*open squares*) and AtAPSK·SO_4^{2-} (*closed squares*) with APS. *D*, titration of AtAPSK G111A with ATPγS (*open squares*) and APS (*closed squares*). Titrations of the G113A mutant yielded similar results. Representative experimental data for the SO_4^{2-} (*A*), AtAPSK/ATPγS (*B*), AtAPSK·SO_4^{2-}/APS (*C*), and G111A/APS (*D*) titrations are plotted as heat signal (µcal s^{-1}) *versus* time (min) in each *upper panel*. Each experiment consisted of 20 to 30 injections of 10 µl each of nucleotide or oxyanion into a solution containing protein. Each *lower panel* shows the integrated heat responses per injection. The *solid line* is the linear regression fit using either a one- or two-site binding model (see Table 4).

TABLE 4

Thermodynamic parameters of APS binding to the AtAPSK·SO_4^{2-} complex, G111A, and G113A proteins

All titrations were performed at 17 °C as described under "Experimental Procedures." ITC data were fit to either a one-site binding model (n = number of sites) or a two-site binding model.

Protein	Titrant	K_1	K_2	ΔH_1	ΔH_2
		µM		*kcal mol*$^{-1}$	
AtAPSK·SO_4^{2-}	APS	3.78 ± 2.55 n = 1.98 ± 0.04		−8.0 ± 0.6	
AtAPSK G111A	APS	102.7 ± 30.1	439.0 ± 131.8	−6.4 ± 2.2	−2.7 ± 1.9
AtAPSK G113A	APS	130.0 ± 45.6	365.9 ± 93.7	−9.1 ± 4.6	−5.4 ± 2.5

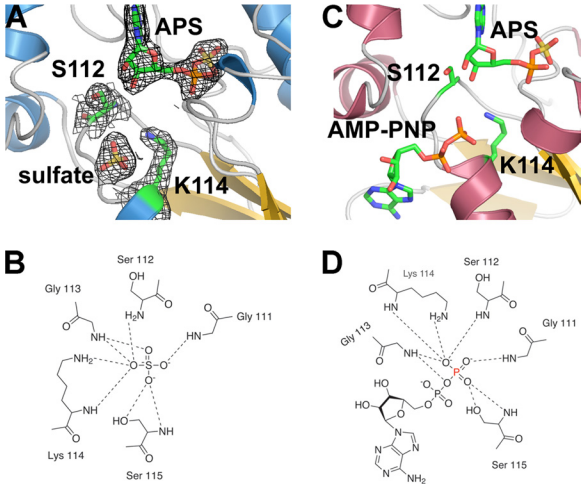

FIGURE 5. **Structure of the AtAPSK·APS·SO_4^{2-} complex.** *A*, active site view showing the $|2F_o - F_c|$ omit map (1.5 σ) for APS and SO_4^{2-}. In addition, the density for Ser^{112} and Lys^{114} in the P-loop are shown. *B*, schematic of interactions made by P-loop residues and SO_4^{2-} in the AtAPSK·APS·SO_4^{2-} complex. *C*, active site view of the AtAPSK·AMP-PNP·APS complex (25, PDB 3UIE) showing positions of bound ligands. *D*, schematic of interactions made by P-loop residues and the β-phosphate of AMP-PNP in the AtAPSK (25); the γ-phosphate is not shown for clarity.

with the potential to mediate communication between the ATP/ADP and APS/PAPS binding sites with the aim of using mutagenesis to alter the effect of ADP on APS binding and to reduce substrate inhibition. At the interface of the two nucleotide-binding sites in AtAPSK (Fig. 6) and the enzyme from other species (25–30), the P-loop (Ser^{110}–Thr^{116}) is essential for ATP/ADP binding and residues from the α3 helix provide critical contacts with APS. In particular, Arg^{141} forms charge-charge interactions with the phosphosulfate group of APS and Asp^{138} provides a bidentate interaction with the hydroxyl groups of the APS ribose and serves as a general base in the reaction mechanism (25, 29). Asp^{136} anchors an extensive network of contacts with Ser^{115} in the P-loop, waters coordinated to Mg^{2+}, and the main chain nitrogen of Asp^{138} in the α3 helix; no other residue in the active site connects multiple structural features.

To examine the role of Asp^{136}, the D136N and D136A mutants were generated, purified, and kinetically characterized. The AtAPSK D136N and D136A mutants displayed 9- and 18-fold reductions in catalytic efficiencies (k_{cat}/K_m), respectively, that primarily resulted from reduced turnover rates (Table 5). The D136A mutant also abolished the effect of substrate inhibition by APS, which prompted us to examine nucleotide binding in this protein. ITC analysis of nucleotide binding to D136A showed that the mutation had little effect on ATP, ATPγS, AMP-PNP, and ADP binding either in the presence or absence of Mg^{2+}, as all these ligands displayed exothermic heat signatures and affinities comparable with wild-type protein (Fig. 7*A*, Table 6). Although Asp^{136} does not directly contact APS, the D136A mutant displayed drastically reduced affinity for APS compared with the wild-type enzyme (Fig. 7*B*). Changes in enthalpy were observed upon titrating the D136A mutant with APS, but the binding isotherms were essentially

linear and precluded an accurate fitting to determine binding affinity. In contrast to the addition of single nucleotides, preincubation of the D136A mutant with either AMP-PNP or ADP followed by addition of APS showed that the affinity for the second ligand was comparable with that observed for wild-type (Fig. 7*C*, Table 6). These results implicate Asp^{136} as required for AtAPSK to bind APS with significant affinity in the absence of ADP or AMP-PNP, as this mutation specifically decreases the affinity for APS in the absence of additional nucleotides without affecting the energetics and affinity for binding in the ATP/ADP site. The AtAPSK D136A mutant exhibits a strict binding order due to the diminished affinity of the enzyme for APS, but not ATP, and suggests that APS binding before ATP is inhibitory to the wild-type enzyme.

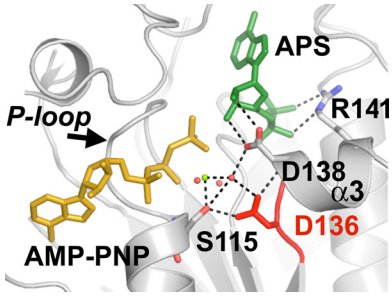

FIGURE 6. **Structural view of the AtAPSK active site.** The positions of APS (*green*) and AMP-PNP (*yellow*) are shown in relationship to residues from the P-loop (Ser^{115}) and residues on or near the α3 helix (Asp^{136}, Asp^{138}, and Arg^{141}) that interact with either APS or the water network (*red spheres*) that coordinates the Mg^{2+} (*green sphere*) are shown. Asp^{136} is highlighted in *red* to emphasize its location between the P-loop and α3 helix. The figure was generated using the AtAPSK·AMP-PNP·APS complex structure (25).

DISCUSSION

Substrate inhibition by APS is a hallmark feature of APSK from bacteria, fungi, plants, and mammals and has been examined using kinetic and structural approaches (7, 20–24, 30), which suggest different models for nucleotide binding (Fig. 1*A*). To date, the thermodynamic basis for the order of ligand binding and how the ATP/ADP and APS/PAPS binding sites interact remains unclear. The combined calorimetric, crystallographic, and kinetic analyses presented here reveal a highly integrated system of dynamic structural and nucleotide recognition features in APSK.

Calorimetric analysis of ligand binding to form AtAPSK binary and ternary nucleotide complexes provides new insight on the interaction between the ATP/ADP and APS/PAPS binding sites within the monomer and helps to define the molecular basis for the proposed ordered sequential mechanism of binding. Steady-state kinetic analysis of APSK from *P. chrysogenum*

TABLE 5

Steady-state kinetic parameters of wild-type and mutant AtAPSK

Average values ± S.E. ($n = 3$) are shown.

Protein	k_{cat}	K_m^{APS}	K_i^{APS}	k_{cat}/K_m
	s^{-1}	μM		$M^{-1}\,s^{-1} \times 10^8$
AtAPSK	272 ± 39	0.48 ± 0.41	37.5 ± 6.9	5.67
AtAPSK D136N	45.0 ± 3.5	0.70 ± 0.29	32.8 ± 7.7	0.64
AtAPSK D136A	29.0 ± 5.1	0.92 ± 0.63		0.31

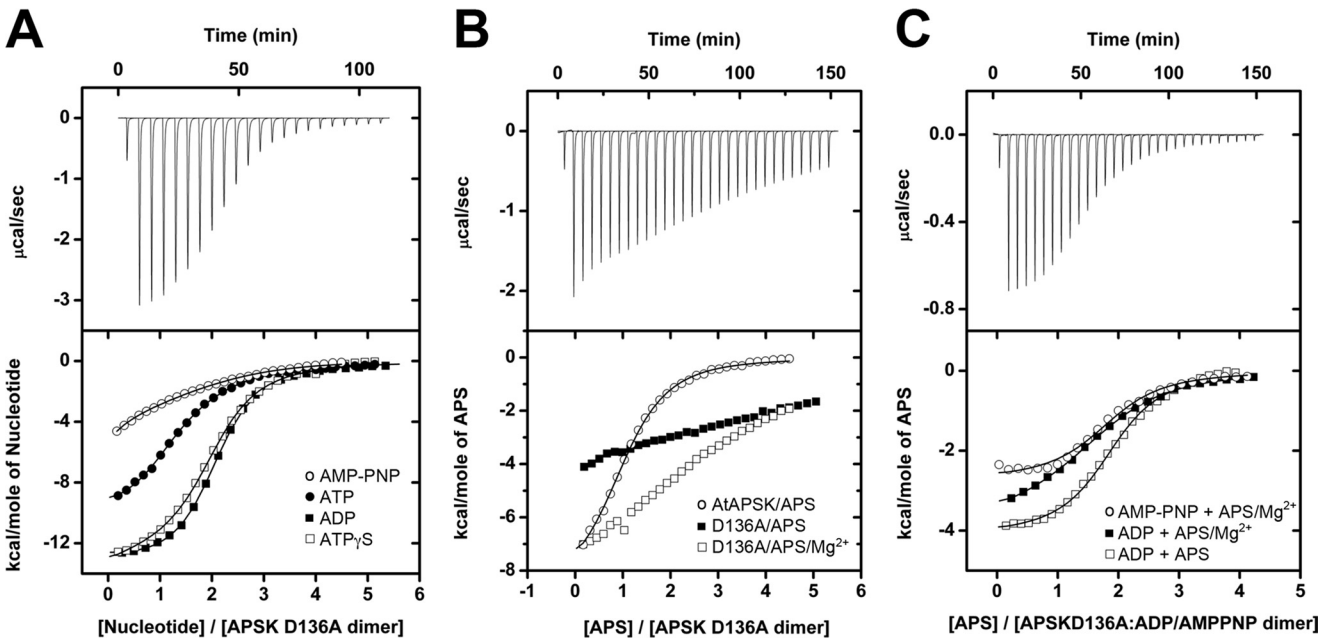

FIGURE 7. **ITC analysis of nucleotide binding to AtAPSK D136A.** *A*, titration of AtAPSK D136A with ADP (*solid squares*), ATPγS (*open squares*), ATP (*closed circles*), and AMP-PNP (*open circles*). *B*, titration of AtAPSK D136A with APS (*solid squares*), APS + 5 mM Mg^{2+} (*open squares*), and AtAPSK with APS (*open circles*). *C*, titration of AtAPSK D136A·ADP with APS (*open squares*), APS + 5 mM Mg^{2+} (*solid squares*), and AtAPSK D136A·AMP-PNP (*open circles*) with APS + 5 mM Mg^{2+}. Representative experimental data for the ADP (*A*) and APS (*B* and *C*) titrations are plotted as heat signal ($\mu cal\ s^{-1}$) *versus* time (min) in each *upper panel*. Each experiment consisted of 20 to 30 injections of 10 μl each of nucleotide into a solution containing AtAPSK dimer. Each *lower panel* shows the integrated heat responses per injection. The *solid line* is the linear regression fit using a two-site binding model (see Table 6).

TABLE 6

Thermodynamic comparison of nucleotide binding to AtAPSK D136A and AtAPSK D136A·nucleotide complexes

All titrations were performed at 17 °C as described under "Experimental Procedures." AtAPSK D136A·nucleotide complexes were pre-formed either in the absence or presence of 5 mM Mg^{2+}. ITC data were fit to either a one-site binding model (n = number of sites) or a two-site binding model.

Pre-bound nucleotide	titrant	K_1	K_2	ΔH_1	ΔH_2
		μM		*kcal mol*$^{-1}$	
	ATP	1.60 ± 0.50	23.6 ± 3.1	−9.0 ± 0.6	−4.2 ± 0.8
	ATPγS	0.80 ± 0.50	10.9 ± 5.8	−11.6 ± 2.7	−8.6 ± 1.4
	AMP-PNP	36.9 ± 6.2	48.0 ± 10.4	−5.0 ± 1.6	−2.2 ± 0.9
	ADP	0.17 ± 0.02	3.40 ± 1.10	−13.2 ± 0.9	−6.3 ± 0.5
	ADP + 5 mM Mg^{2+}	0.41 ± 0.02	6.0 ± 1.3	−12.8 ± 1.4	−9.7 ± 2.2
AMP-PNP	APS	5.3 ± 0.5 n = 1.95 ± 0.04		−2.7 ± 0.1	
AMP-PNP + 5 mM Mg^{2+}	APS	6.0 ± 0.3 n = 2.08 ± 0.07		−2.3 ± 0.1	
ADP	APS	4.0 ± 0.5 n = 2.10 ± 0.10		−4.1 ± 0.4	
ADP + 5 mM Mg^{2+}	APS	1.80 ± 0.20	11.1 ± 0.9	−3.5 ± 0.4	−2.6 ± 0.5

and *E. coli* suggest alternative models for the order of ligand addition (Fig. 1*A*) (20, 21). As shown here, ATP, AMP-PNP, ATPγS, ADP, and APS all bind to AtAPSK with APS binding displaying the weakest affinity (Fig. 2, Table 2). Analysis of ternary complex formation shows that ordered addition of AMP-PNP enhances the affinity for APS by 50-fold (Fig. 3, Table 3). In contrast, addition of AMP-PNP to the AtAPSK·APS complex does not significantly change affinity. Moreover, the tighter binding of ADP compared with ATP and its analogs to either unliganded AtAPSK or the AtAPSK·APS complex confirms that substrate inhibition results from facile formation of a dead-end form of the enzyme (22, 24, 30).

Although binding of nucleotides to AtAPSK can occur in either order, the two possible routes leading to formation of the AtAPSK·ATP·APS ternary complex are not thermodynamically equivalent. For example, addition of ATP first followed by APS showed exothermic binding interactions (K_d = 1.50 μM; ΔH = −3.3 kcal mol^{-1}; ΔG = +7.73 kcal mol^{-1}; $-T\Delta S$ = 11.0 kcal mol^{-1}), whereas addition of APS followed by AMP-PNP was endothermic (K_d = 3.10 μM; ΔH = +4.3 kcal mol^{-1}; ΔG = +7.31 kcal mol^{-1}; $-T\Delta S$ = 3.0 kcal mol^{-1}) (Fig. 3, Table 3). The enthalpic changes are offset by concomitant entropic changes that maintain binding affinity. This difference in the binding energetics of the two reaction sequences likely reflects structural changes in the active site that correspond to the order of ligand addition, which are discussed below. Overall, these results are consistent with a preferred order of ligand binding in APSK, in which ATP binds first followed by APS, and the proposed ordered sequential mechanism determined by steady-state kinetics (20).

The ITC data presented here also supports a previous suggestion of cross-talk between active sites within the APSK homodimer based on crystallographic studies (25, 39). Single nucleotide titrations of AtAPSK yielded binding isotherms best fit by a two-site model in which the K_d values for the second site were 5–30-fold higher than the first site for each nucleotide (Fig. 2, Table 2). Moreover, pre-ordering of the active site by formation of a binary complex before nucleotide addition either reduces or eliminates the effectiveness of potential communication within the dimer (Fig. 3, Table 3). The lack of binding asymmetry for formation of the ternary complexes suggests that preincubation with ligands occupies the binding site and organizes the active sites in the dimer for a more symmetric interaction with the second nucleotide. Although the molecular basis of this effect needs to be further examined, the N-terminal region of APSK has been implicated as a possible control feature for this behavior. Earlier crystallographic studies of the APSK domain from human PAPS synthetase revealed asymmetry in substrate binding between monomers of the protein (30, 39). This led to the suggestion that nucleotide binding in one active site alters the position of the N-terminal domain adjacent to the monomer, which entwines the other monomer (Fig. 1*B*), to provide a "coupling function" that communicates nucleotide occupancy between active sites (30). A similar asymmetry was observed in the disulfide linkages of the N-terminal domain of the AtAPSK·AMP-PNP·APS complex (25). The dynamic nature of structural features of APSK is also underscored by the nucleotide binding analyses presented above and by the effects of mutations in the P-loop and Asp^{136} in the active site.

As in other ATP-dependent enzymes, the P-loop of APSK is critical for enzymatic function (40, 41). Binding AMP-PNP, ADP, or SO_4^{2-} in the ATP/ADP site results in increased affinity of AtAPSK for APS (Tables 3 and 4). In multiple crystal structures, AMP-PNP and ADP interact with residues in the P-loop (Fig. 5), which provides a driving force for nucleotide recognition as it forms nine hydrogen bonds with the β-phosphate compared with two hydrogen bonds made between the rest of the nucleotide and protein (23–30). Comparable interactions are observed for SO_4^{2-} bound in the AtAPSK·APS·SO_4^{2-} complex (Fig. 5). To examine the role of the P-loop in determining binding order, nucleotide binding to two AtAPSK mutants (G111A and G113A) was examined (Fig. 4*D*, Table 4). The resultant isotherms from titrations with either ATPγS or ADP could not be fit to obtain binding constants, but APS binding was comparable that of the wild-type apoenzyme (Table 1). Based on the energetic analysis of wild-type and mutant AtAPSK, interactions made between ATP and the P-loop help order the active site and position the γ-phosphate in proximity to APS for catalysis.

This work also identifies Asp^{136} as a critical determinant for determining the order of nucleotide binding and for APS substrate inhibition. The position of Asp^{136} in the AtAPSK active site anchors an extensive set of interactions that connect the P-loop and the α3-helix in the APS binding site (Fig. 6). Steady-state kinetic characterization of the D136N and D136A mutants reveals a modest change in catalytic efficiency, but a loss of substrate inhibition by APS in the D136A mutant (Table 5). Thus, kinetic analysis would suggest a minor role for this residue; however, examination of nucleotide binding in the D136A mutant by ITC reveals a critical role for guiding ligand

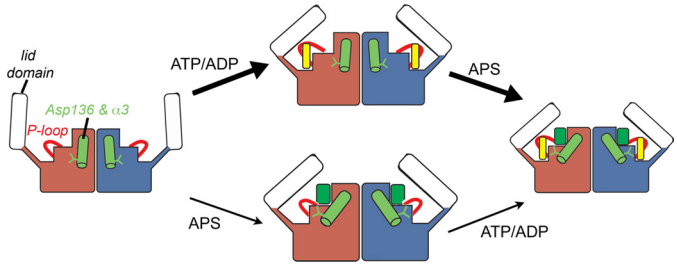

FIGURE 8. **Model for ligand binding to AtAPSK.** The structure of AtAPSK is shown as a schematic with the core domain of each monomer colored *rose* and *blue*, respectively, and the lid domain colored *white*. The P-loop is shown as a *red loop* with Asp^{136} and the α3-helix in *green*. Ligands are indicated by *colored rectangles* in each binding site as follows: ATP (*yellow rectangle*) and APS (*green rectangle*). *Thicker arrows* indicate the preferred order of ligand binding.

binding. Mutation of Asp^{136} to an alanine drastically reduced the K_d for APS without altering binding at the ATP/ADP site (Fig. 7, Table 6), even though this residue does not directly contact APS. In contrast, the D136A mutant showed a slightly decreased affinity for APS after formation of the AtAPSK-D136A·AMP-PNP complex. This demonstrates that the D136A mutation affects ligand addition to effectively allow only an ordered sequential binding of ATP and then APS, not vice versa. These results suggest a structural model for distinguishing the order of nucleotide binding to APSK (Fig. 8).

Crystallographic studies of the unliganded and nucleotide bound forms of APSK indicate that the mobile active site capping or lid domain binds to the P-loop and provides interactions with APS to lock substrates into the active site (23, 26). It is unclear what coordinates the movement of this domain with nucleotide binding, but loop and ligand interactions likely alter the flexibility of this loop. Based on the ITC analysis presented here, binding of ATP·Mg^{2+} to AtAPSK first pre-organizes the active site for subsequent addition of APS (Fig. 8, *top*). ATP binding establishes extensive interactions between the β-phosphate and P-loop and places the γ-phosphate in proximity to the acceptor hydroxyl group of APS once bound, and helps position Asp^{136} to bridge Ser^{115} in the P-loop, the water molecules coordinating the Mg^{2+} ion, and the α3 helix to bring Asp^{138} and Arg^{141} into proximity for APS binding and phosphoryl-group transfer. These results imply highly interconnected roles for the P-loop and Asp^{136} that allow for energetically efficient formation of the AtAPSK·ATP·APS ternary complex and ensuing catalysis. In contrast, initial APS binding is possible (Fig. 8, *bottom*), but alters movement of the lid domain and P-loop for subsequent ATP binding, as suggested by the thermodynamic differences associated with the AMP-PNP binding to the AtAPSK·APS complex (Fig. 3*C*, Table 3). Thus, APS binding first has an overall inhibitory effect on the reaction sequence and changes the energetics that allow optimal active site conformation. These studies of AtAPSK suggest an important role for the dynamic motions of active site features in response to ligand binding order. As recently shown for adenylate kinase (42, 43), movement in localized structures can preferentially create active site configurations that favor efficient catalysis. A similar series of events can now be proposed for the APSK reaction mechanism.

Acknowledgments—Portions of this research were carried out at the Argonne National Laboratory Structural Biology Center of the Advanced Photon Source, a national user facility operated by the University of Chicago for the Dept. of Energy Office of Biological and Environmental Research (DE-AC02–06CH11357).

REFERENCES

1. Schelle, M. W., and Bertozzi, C. R. (2006) Sulfate metabolism in mycobacteria. *ChemBioChem* **7,** 1516–1524
2. Patron, N. J., Durnford, D. G., and Kopriva, S. (2008) Sulfate assimilation in eukaryotes. Fusions, relocations, and lateral transfers. *BMC Evol. Biol.* **8,** 39
3. Yi, H., Galant, A., Ravilious, G. E., Preuss, M. L., and Jez, J. M. (2010) Sensing sulfur conditions. Simple to complex protein regulatory mechanisms in plant thiol metabolism. *Mol. Plant* **3,** 269–279
4. Yi, H., Ravilious, G. E., Galant, A., Krishnan, H. B., and Jez, J. M. (2010) From sulfur to homoglutathione. Thiol metabolism in soybean. *Amino Acids* **39,** 963–978
5. Takahashi, H., Kopriva, S., Giordano, M., Saito, K., and Hell, R. (2011) Sulfur assimilation in photosynthetic organisms. Molecular functions and regulations of transporters and assimilatory enzymes. *Annu. Rev. Plant Biol.* **62,** 157–184
6. Ravilious, G. E., and Jez, J. M. (2012) Structural biology of plant sulfur metabolism. From assimilation to biosynthesis. *Nat. Prod. Rep.,* in press
7. Lillig, C. H., Schiffmann, S., Berndt, C., Berken, A., Tischka, R., and Schwenn, J. D. (2001) Molecular and catalytic properties of *Arabidopsis thaliana* adenylyl sulfate (APS) kinase. *Arch. Biochem. Biophys.* **392,** 303–310
8. Klein, M., and Papenbrock, J. (2004) The multiprotein family of *Arabidopsis* sulfotransferases and their relatives in other plant species. *J. Exp. Bot.* **55,** 1809–1820
9. Halkier, B. A., and Gershenzon, J. (2006) Biology and biochemistry of glucosinolates. *Annu. Rev. Plant Biol.* **57,** 303–333
10. Amano, Y., Tsubouchi, H., Shinohara, H., Ogawa, M., and Matsubayashi, Y. (2007) Tyrosine-sulfated glycopeptide involved in cellular proliferation and expansion in *Arabidopsis*. *Proc. Natl. Acad. Sci. U.S.A.* **104,** 18333–18338
11. Mugford, S. G., Yoshimoto, N., Reichelt, M., Wirtz, M., Hill, L., Mugford, S. T., Nakazato, Y., Noji, M., Takahashi, H., Kramell, R., Gigolashvili, T., Flügge, U. I., Wasternack, C., Gershenzon, J., Hell, R., Saito, K., and Kopriva, S. (2009) Disruption of adenosine 5′-phosphosulfate kinase in *Arabidopsis* reduces levels of sulfated secondary metabolites. *Plant Cell* **21,** 910–927
12. Kopriva, S., Mugford, S. G., Matthewman, C., and Koprivova, A. (2009) *Arabidopsis* root growth dependence on glutathione is linked to auxin transport. *Plant Cell Rep.* **28,** 1769–1780
13. Mugford, S. G., Matthewman, C. A., Hill, L., and Kopriva, S. (2010) Adenosine 5′-phosphosulfate kinase is essential for *Arabidopsis* viability. *FEBS Lett.* **584,** 119–123
14. Yatusevich, R., Mugford, S. G., Matthewman, C., Gigolashvili, T., Frerigmann, H., Delaney, S., Koprivova, A., Flügge, U. I., and Kopriva, S. (2010) Genes of primary sulfate assimilation are part of the glucosinolate biosynthetic network in *Arabidopsis thaliana*. *Plant J.* **62,** 1–11
15. Chen, H., Zhang, B., Hicks, L. M., and Xiong, L. (2011) A nucleotide metabolite controls stress-responsive gene expression and plant development. *PLoS One* **6,** e26661
16. Bick, J. A., Setterdahl, A. T., Knaff, D. B., Chen, Y., Pitcher, L. H., Zilinskas, B. A., and Leustek, T. (2001) Regulation of plant-type 5′-adenylyl sulfate reductase by oxidative stress. *Biochemistry* **40,** 9040–9048
17. Martin, M. N., Tarczynski, M. C., Shen, B., and Leustek, T. (2005) The role of 5′-adenylylsulfate reductase in controlling sulfate reduction in plants. *Photosynth. Res.* **86,** 309–323
18. Loudet, O., Saliba-Colombani, V., Camilleri, C., Calenge, F., Gaudon, V., Koprivova, A., North, K. A., Kopriva, S., and Daniel-Vedele, F. (2007) Natural variation for sulfate content in *Arabidopsis thaliana* is highly controlled by APR2. *Nat. Genet.* **39,** 896–900
19. Scheerer, U., Haensch, R., Mendel, R. R., Kopriva, S., Rennenberg, H., and

Herschbach, C. (2010) Sulfur flux through the sulfate assimilation pathway is differently controlled by adenosine 5′-phosphosulphate reductase under stress and in transgenic poplar plants overexpressing γECS, SO, or APR. *J. Exp. Bot.* **61,** 609–622
20. Renosto, F., Seubert, P. A., Knudson, P., and Segel, I. H. (1985) Adenosine 5′-phosphosulfate kinase from *Penicillium chrysogenum.* Determining ligand dissociation constants of binary and ternary complexes from the kinetics of enzyme inactivation. *J. Biol. Chem.* **260,** 11903–11913
21. Satishchandran, C., and Markham, G. D. (2000) Mechanistic studies of *Escherichia coli* adenosine 5′-phosphosulfate kinase. *Arch. Biochem. Biophys.* **378,** 210–215
22. Renosto, F., Martin, R. L., and Segel, I. H. (1991) Adenosine 5′-phosphosulfate kinase from *Penicillium chrysogenum.* Ligand binding properties and the mechanism of substrate inhibition. *Arch. Biochem. Biophys.* **284,** 30–34
23. Lansdon, E. B., Segel, I. H., and Fisher, A. J. (2002) Ligand-induced structural changes in adenosine 5′-phosphosulfate kinase from *Penicillium chrysogenum. Biochemistry* **41,** 13672–13680
24. MacRae, I. J., and Segel, I. H. (1999) Adenosine 5′-phosphosulfate (APS) kinase, diagnosing the mechanism of substrate inhibition. *Arch. Biochem. Biophys.* **361,** 277–282
25. Ravilious, G. E., Nguyen, A., Francois, J. A., and Jez, J. M. (2012) Structural basis and evolution of redox regulation in plant adenosine 5′-phosphosulfate kinase. *Proc. Natl. Acad. Sci. U.S.A.* **109,** 309–314
26. MacRae, I. J., Segel, I. H., and Fisher, A. J. (2000) Crystal structure of adenosine 5′-phosphosulfate kinase from *Penicillium chrysogenum. Biochemistry* **39,** 1613–1621
27. Yu, Z., Lansdon, E. B., Segel, I. H., and Fisher, A. J. (2007) Crystal structure of the bifunctional ATP sulfurylase-APS kinase from the chemolithotrophic thermophile *Aquifex aelicus. J. Mol. Biol.* **365,** 732–743
28. Gay, S. C., Segel, I. H., and Fisher, A. J. (2009) Structure of the two-domain hexameric APS kinase from *Thiobacillus denitrificans.* Structural basis for the absence of ATP sulfurylase activity. *Acta Crystallogr. D Biol. Crystallogr.* **65,** 1021–1031
29. Sekulic, N., Dietrich, K., Paarmann, I., Ort, S., Konrad, M., and Lavie, A. (2007) Elucidation of the active conformation of the APS-kinase domain of human PAPS synthetase 1. *J. Mol. Biol.* **367,** 488–500
30. Sekulic, N., Konrad, M., and Lavie, A. (2007) Structural mechanism for substrate inhibition of the adenosine 5′-phosphosulfate kinase domain of human 3′-phosphoadenosine-5′-phosphosulfate synthetase 1 and its ramifications for enzyme regulation. *J. Biol. Chem.* **282,** 22112–22121
31. Walker, J. E., Saraste, M., Runswick, M. J., and Gay, N. J. (1982) Distantly related sequences in the α- and β-subunits of ATP synthase, myosin, kinases, and other ATP-requiring enzymes and a common nucleotide binding fold. *EMBO J.* **1,** 945–951
32. Saraste, M., Sibbald, P. R., and Wittinghofer, A. (1990) The P-loop, a common motif in ATP- and GTP-binding proteins. *Trends Biochem. Sci.* **15,** 430–434
33. Phartiyal, P., Kim, W. S., Cahoon, R. E., and Jez, J. M. (2006) Soybean ATP sulfurylase, a homodimeric enzyme involved in sulfur assimilation, is abundantly expressed in roots and induced by cold treatment. *Arch. Biochem. Biophys.* **450,** 20–29
34. Kumaran, S., Yi, H., Krishnan, H. B., and Jez, J. M. (2009) Assembly of the cysteine synthase complex and the regulatory role of protein-protein interactions. *J. Biol. Chem.* **284,** 10268–10275
35. Minor, W., Cymborowski, M., Otwinowski, Z., and Chruszcz, H. (2006) HKL-3000, the integration of data reduction and structure solution. From diffraction images to an initials model in minutes. *Acta Crystallogr. D Biol. Crystallogr.* **62,** 859–866
36. McCoy, A. J., Grosse-Kunstleve, R. W., Adams, P. D., Winn, M. D., Storoni, L. C., and Read, R. J. (2007) Phaser crystallographic software. *J. Appl. Crystallogr.* **40,** 658–674
37. Emsley, P., Lohkamp, B., Scott, W. G., and Cowtan, K. (2010) Features and developmen of COOT. *Acta Cryststallogr. D Biol. Crystallogr.* **66,** 486–501
38. Adams, P. D., Afonine, P. V., Bunkóczi, G., Chen, V. B., Davis, I. W., Echols, N., Headd, J. J., Hung, L. W., Kapral, G. J., Grosse-Kunstleve, R. W., McCoy, A. J., Moriarty, N. W., Oeffner, R., Read, R. J., Richardson, D. C., Richardson, J. S., Terwilliger, T. C., and Zwart, P. H. (2010) PHENIX, a comprehensive Python-based system for macromolecular structure solution. *Acta Crystallogr. D Biol. Crystallogr.* **66,** 213–221
39. Harjes, S., Bayer, P., and Scheidig, A. J. (2005) The crystal structure of human PAPS synthetase 1 reveals asymmetry in substrate binding. *J. Mol. Biol.* **347,** 623–635
40. Deyrup, A. T., Krishnan, S., Cockburn, B. N., and Schwartz, N. B. (1998) Deletion and site-directed mutagenesis of the ATP-binding motif (P-loop) in the bifunctional murine ATP-sulfurylase/adenosine 5′-phosphosulfate kinase enzyme. *J. Biol. Chem.* **273,** 9450–9456
41. MacRae, I. J., Rose, A. B., and Segel, I. H. (1998) Adenosine 5′-phosphosulfate kinase from *Penicillium chrysogenum.* Site-directed mutagenesis at putative phosphoryl-accepting and ATP P-loop residues. *J. Biol. Chem.* **273,** 28583–28589
42. Henzler-Wildman, K. A., Thai, V., Lei, M., Ott, M., Wolf-Watz, M., Fenn, T., Pozharski, E., Wilson, M. A., Petsko, G. A., Karplus, M., Hübner, C. G., and Kern, D. (2007) Intrinsic motions along an enzymatic reaction trajectory. *Nature* **450,** 838–844
43. Henzler-Wildman K., and Kern, D. (2007) Dynamic personalities of proteins. *Nature* **450,** 964–972